Materials Advances

ROYAL SOCIETY OF CHEMISTRY

PAPER

View Article Online
View Journal | View Issue

Cite this: *Mater. Adv.*, 2022, 3, 4006

Searching for better X-ray and γ-ray photodetectors: structure–composition properties of the $TlPb_2Br_{5-x}I_x$ quaternary system†

M. Piasecki,*[ab] O. V. Parasyuk,[c] V. Pavlyuk,[ad] O. Y. Khyzhun,[e] I. V. Kityk,[fg] G. L. Myronchuk,[g] K. T. Wojciechowski,[h] S. I. Levkovets,[c] L. V. Piskach,[c] A. O. Fedorchuk,[i] P. M. Fochuk,[j] V. Wood[k] and M. Yarema*[k]

Developing X-ray and γ-ray detectors with stable operation at ambient temperature and high energy resolution is an open challenge. Here, we present an approach to search for new detector materials, combining binary photodetector compounds. More specifically, we explore quaternary $TlPb_2Br_{5-x}I_x$ compositions, relying on materials synergy between TlBr, TlI, and PbI_2 photodetectors. We discover a broad solid solution in the $TlPb_2Br_5$–'$TlPb_2I_5$' section, which can be derived from a new quaternary compound, $TlPb_2BrI_4$, by partial substitution of Br by I atoms on the 4c site or by replacement of I by Br atoms on the 16l site. We carry out a thorough crystallographic analysis of the new $TlPb_2BrI_4$ compound and prepare a high-quality standardized structure file. We also complete the phase diagram of the $TlPb_2Br_5$–'$TlPb_2I_5$' section, based on 21 alloys. Furthermore, we synthesize a series of high quality centimeter-sized $TlPb_2Br_{5-x}I_x$ single crystals (x = 2, 2.5, 3, 3.5, 4, 4.5) by the Bridgman–Stockbarger method and study their structure and properties using a combination of experimental techniques (X-ray diffraction, X-ray photoelectron spectroscopy, and absorption spectroscopy) and theoretical calculations.

Received 31st December 2021,
Accepted 22nd March 2022

DOI: 10.1039/d1ma01259b

rsc.li/materials-advances

Introduction

Room-temperature X-ray and γ-ray photodetectors are advantageous for a wide range of medical and industrial applications. There is, however, a limited number of materials, which can be utilized in such photodetectors, due to several stringent requirements (*i.e.*, high average atomic number, large physical density, large electrical resistance, wide optical band gap, and high value for a merit factor $\mu\cdot\tau$, where μ is carrier mobility and τ is lifetime).[1] Furthermore, ease of synthesis and quality of the obtained crystals imply additional limits. Apparently, none of the existing detector materials meets all the requirements, which stimulates the search for new detector materials.

Currently, the most known and commonly used materials are CdTe and $Cd_xZn_{1-x}Te$ (CZT), featuring high energy resolution and stable operation at ambient temperature.[2] However, despite decades of research, the spatial homogeneity of CdTe and CZT crystals is insufficient, particularly for larger size detector applications, while the fabrication of such large telluride crystals is also expensive.[3] Thallium bromide (TlBr) detector material has a number of advantages with respect to CZT, including higher density, higher atomic numbers, and larger energy band gap. Moreover, the relatively low melting temperature of TlBr enables large high-quality crystals *via*

[a] *J.Dlugosz University Częstochowa, Armii Krajowej 13/15, Częstochowa, Poland. E-mail: piasecki@ujd.edu.pl*
[b] *Inorganic Chemistry Department, Uzhhorod National University, 46 Pidhirna, Uzhhorod, Ukraine*
[c] *Department of Inorganic and Physical Chemistry, Eastern European National University, Voli Ave. 13, Lutsk, Ukraine*
[d] *Department of Inorganic Chemistry, Ivan Franko National University, Kyryla i Mefodiya Str. 6, Lviv, Ukraine*
[e] *Frantsevych Institute for Problems of Materials Science, National Academy of Sciences of Ukraine, 3 Krzhyzhanivsky St., Kyiv, Ukraine*
[f] *Electrical Engineering Department, Czestochowa University Technology, Armii Krajowej 17, Czestochowa, Poland*
[g] *Department of Experimental Physics and Information-Measuring Technology, Lesya Ukrainka Eastern European National University, 13 Voli Avenue, Lutsk, Ukraine*
[h] *Thermoelectric Research Laboratory, Department of Inorganic Chemistry, Faculty of Materials Science and Ceramics, AGH University of Science and Technology, 30 Mickiewicza Avenue, Krakow, Poland*
[i] *Department of Inorganic and Organic Chemistry, Lviv National University of Veterinary Medicine and Biotechnologies, Pekarska St. 50, Lviv, Ukraine*
[j] *Yuriy Fed'kovych Chernivtsi National University, 2 Kotziubynskoho St., Chernivtsi, Ukraine*
[k] *Institute for Electronics, Department of Information Technology and Electrical Engineering, ETH Zurich, Gloriastrasse 35, Zurich, Switzerland. E-mail: yaremam@ethz.ch*

† Electronic supplementary information (ESI) available: Overview table of X-ray and γ-ray photodetectors, photos of single crystals, Rietveld refinement images and tables, and survey XPS spectra. See https://doi.org/10.1039/d1ma01259b

convenient melt methods. The disadvantages of thallium bromide crystals, however, include relatively pure mechanical stability and high sensitivity to polarization effects.[4] These apply to other binary halides, PbI_2 and HgI_2, which are used as detector materials. Apart from poor mechanical properties, PbI_2 and HgI_2 detectors are unstable in time, and their $\mu\cdot\tau$ values are lower compared to those of TlBr and CZT detectors.[5–8] Recently, many ternary and quaternary materials have been studied as room-temperature X-ray and γ-ray photodetectors (Table S1, ESI†). Among others, ternary halides and chalcohalides exhibit promising characteristics (*e.g.*, merit factors $\mu\cdot\tau_e$ and $\mu\cdot\tau_h$ in $CsPbBr_3$,[9] $CsPbCl_3$,[10] Tl_4CdI_6,[1] Tl_6SeI_4,[11] and Tl_6SI_4[12] are on par with those of classical detector materials).

In this paper, we investigate quaternary $TlPb_2Br_{5-x}I_x$ compositions as a promising system for X-ray and γ-ray photodetector applications. Our approach is based to find principally new material by studying the mutual interaction between binary halides (in this case, TlBr, TlI, and PbI_2). It was found beneficial to mix TlBr and TlI, and $TlBr_xI_{1-x}$ crystals were more mechanically stable compared to TlBr, which is very important to minimize mechanical defects during device manufacturing.[13] Mixing in the PbI_2 moiety can tune the non-optimal optical band gap of $TlBr_xI_{1-x}$ crystals[14] without deterioration of the $\mu\cdot\tau$ merit factor. In line with our rationale, nuclear radiation detection was recently reported for $TlPb_2Br_5$.[15]

We therefore synthesize 21 alloys to explore the $TlPb_2Br_5$–'$TlPb_2I_5$' phase diagram. We detect two solid solutions, high-temperature phases, and new crystallographic structure for the quaternary $TlPb_2BrI_4$ compound. We investigate the structure, and the electronic and optical properties of the new $TlPb_2Br_{5-x}I_x$ materials using a combination of experimental techniques (X-ray diffraction, X-ray photoelectron spectroscopy, and absorption spectroscopy) and theoretical calculations.

Experimental section

Phase diagram of the $TlPb_2Br_5$–'$TlPb_2I_5$' section was determined by investigating the 21 alloys with preselected chemical compositions (Fig. S1 and Table S2, ESI†). These alloys were synthesized by melting the batches, soldered in evacuated quartz ampoules in a shaft-type furnace. The 2 g batches were composed of binary halides; the synthesis method and purification techniques are same as those reported in detail elsewhere.[16–19] Briefly, the ampoules were heated to 870 K at the rate of 30 K h^{-1}. After 6 h of the exposure, alloys were gradually cooled (20 K h^{-1}) to room temperature. The obtained alloys were investigated by the X-ray diffraction (XRD) and differential thermal analysis (DTA) methods. Powder XRD study was performed using a Bruker D8 Advance diffractometer (CuKα-radiation, $10^\circ \le 2\theta \le 110^\circ$, a scan step of 0.005°) and a URD-6 diffractometer (CuKα radiation, $10^\circ \le 2\theta \le 80^\circ$, a scan step of 0.05°). XRD patterns were analyzed using the FullProf software package.[17] The refinement of structural parameters was performed by the Rietveld method (*i.e.*, by comparison of the theoretically calculated and the experimental diffraction patterns). Differential thermal analysis curves were recorded using Netzsch STA 409 in an inert Argon atmosphere.

High-temperature XRD was performed using a Rigaku SmartLab 9 kW System, equipped with a rotating Cu anode and a 2D solid state detector (HyPix-3000 SL). The high-temperature stage (Anton Paar) consists of a ceramic plate, which is shielded with an amorphous carbon dome. The high-temperature XRD measurements were performed in a nitrogen atmosphere. Temperature was controlled with a precision of ±1 °C.

A series of single crystals were obtained for the $TlPb_2Br_{5-x}I_x$ solid solutions with the composition in the range of 40–90 mol% '$TlPb_2I_5$' with a 10 mol% step (*i.e.*, x = 2, 2.5, 3, 3.5, 4, 4.5). The Bridgman–Stockbarger method was used for their growth. The 15 g batches were composed of the calculated amounts of binary halides, placed in the growth containers of quartz glass, evacuated, and then soldered. After pre-annealing in a shaft-type furnace, the containers were transferred to the pre-heated two-zone growth furnaces. The temperature of the upper zone was about 700 K, and that of the bottom zone was 520 K. After melting the alloys, the procedure required for the formation of a seed crystal was performed. About 4–5 mm of the melt was crystallized followed by the recrystallization annealing for 50 h. Then 2–3 mm of the seed was melted, and the crystal was gradually grown by slowly lowering (2 mm per day) the ampoule into the bottom furnace. The temperature gradient at the solid–melt interface was 12 K cm^{-1}. After the complete crystallization of the melt, the furnace was cooled at the rate of 5 K h^{-1} to room temperature. The single crystals of the $TlPb_2Br_5$–'$TlPb_2I_5$' section obtained are shown in Fig. S2 (ESI†). The color of the $TlPb_2Br_{5-x}I_x$ crystals changes with increasing iodine content from yellow to light-brown. The obtained crystals were characterized by powder XRD and X-ray photoelectron spectroscopy (XPS).

Crystals with parallel-plane high optical-quality surfaces of 0.05–0.08 mm thickness were used for optical measurements. The surfaces were mechanically polished with diamond pastes of various grain sizes. Absorption spectra were measured using an MDR-208 monochromator with a silicon photosensor. The resolution of the monochromator was 0.3 nm.

The XPS core-level and valence-band spectra of the $TlPb_2Br_{5-x}I_x$ solid solutions were recorded using the UHV-Analysis-System produced by SPECS Surface Nano Analysis Company (Berlin, Germany). The UHV-Analysis-System is supplied with a hemispherical PHOIBOS 150 analyzer and operates at a base pressure less than 7×10^{-10} mbar. The XPS spectra of the $TlPb_2Br_{5-x}I_x$ solutions were excited by a Mg Kα X-ray source (E = 1253.6 eV) and were acquired at a constant pass energy of 25 eV. The calibration technique of the spectrometer energy scale was the same as that reported elsewhere.[20] Since the $TlPb_2Br_{5-x}I_x$ solid solutions are semiconductors, we have taken into account the surface charging effects with reference to the C 1s line (284.6 eV) of adsorbed from laboratory air adventitious carbon as it is recommended for lead-based bromides and iodides.[21–23]

The photoinduced changes in absorption were studied using a He-Cd cw laser at 25 mW beam power as a probing light. A Si

photodetector was used for the monitoring of the reflection light at angles varying within 20–34°. The stability of this laser was equal to about 0.1%. The beam diameter was equal to about 2 mm. The TEM was used for laser control. As a photo-inducing laser we have used a nanosecond Nd:YAG laser (wavelength 1064 nm, pulse duration 8 ns), an Er:glass laser (λ = 1540 nm, time duration 25 ns, pulse frequency repetition 10 Hz) and third harmonic generation of a CO_2 laser. The corresponding polarizer allows varying continuously the power densities up to 1 GW cm^{-2} using rotating polarizers.

Results and discussion

Phase diagram of the $TlPb_2Br_5$–'$TlPb_2I_5$' section

Ternary thallium lead bromide, $TlPb_2Br_5$, belongs to the group of AB_2X_5 compounds, which crystallize in either the monoclinic structure ($NH_4Pb_2Cl_5$ type, space group (SG) $P2_1c$) or the tetragonal one ($NH_4Pb_2Br_5$ type, SG $I4/mcm$). Beck *et al.*[24] have found that the AB_2X_5 structure can be predicted based on the ratio of ionic radii A/X to B/X, according to the structure field chart. Boundary line of the fields is determined by the equation

$$\left(\frac{A}{X}\right)_b = 1.85\left(\frac{B}{X}\right)_b - 0.344 \quad (1)$$

where lower A/X and higher B/X values favor an occurrence of the monoclinic structure type. For the $TlPb_2Br_5$ compound, the ratio Tl^+/Br^- to Pb^{2+}/Br^- lies precisely on the boundary line (eqn (1)). Therefore, the existence of polymorphism is not surprising for this case. Low-temperature (LT) modification LT-$TlPb_2Br_5$ crystallizes in the monoclinic structure (SG $P2_1/c$) with the unit cell parameters a = 9.2957 Å, b = 8.3407 Å, c = 13.013 Å, and β = 89.96°.[16] The structure of high-temperature (HT) modification HT-$TlPb_2Br_5$ is currently not determined.

Phase diagram of the $TlPb_2Br_5$–'$TlPb_2I_5$' section is presented in Fig. 1A. Ternary bromide $TlPb_2Br_5$ melts at 667 K, which is close to the values reported before.[25,26] Partial substitution of Br by I favors the stabilization of the HT-$TlPb_2Br_5$ phase at lower temperatures and leads to the formation of its solid solution that exists in the wide concentration range. At the same time, the main part of phase diagram is the homogeneity region of the new quaternary phase, $TlPb_2Br_{5-x}I_x$. Typical diffraction patterns of alloys in this section are shown in Fig. 1B. The uppermost pattern corresponds to the monoclinic structure of LT-$TlPb_2Br_5$. The same structure is observed for $TlPb_2Br_{4.75}I_{0.25}$ and $TlPb_2Br_{4.25}I_{0.75}$ alloys, which contain 5 mol% and 15 mol% of '$TlPb_2I_5$'. The change of unit cell dimensions (Fig. 1C) shows that the α'-solid solution range of LT-$TlPb_2Br_5$ extends from 0 to ~18 mol% '$TlPb_2I_5$'. In agreement, the diffraction patterns in the range of ~18–24 mol% '$TlPb_2I_5$' (*i.e.*, $TlPb_2Br_{3.9}I_{1.1}$ alloy) contain a superposition of the reflections of two phases. The patterns of alloys in the compositional range of $TlPb_2Br_{3.75}I_{1.25}$–$TlPb_2Br_{0.5}I_{4.5}$ are single-phase and are indexed in the tetragonal structure. A shift of the reflections to lower angles is observed, indicating an increase of the unit cell dimensions of the tetragonal cell (Fig. 1C), due to the substitution of Br^- with larger I^- ions. The single-phase region of γ-solid solution (determined by the lattice period variation) lies in the range of ~24–91 mol% '$TlPb_2I_5$'. The diffraction pattern of 100 mol% '$TlPb_2I_5$' is two-phase and contains the reflections of $TlPbI_3$ and PbI_2 compounds; the pattern of $TlPb_2Br_{0.25}I_{4.75}$ is three-phase, having reflections from γ-solid solution, $TlPbI_3$, and PbI_2.

It should be noted that compound $TlPb_2I_5$ has been reported previously, exhibiting a tetragonal structure with unit cell parameters a = 8.902 Å and c = 15.132 Å.[27] At the same time, other studies of the TlI–PbI_2 phase diagram[28,29] do not report this phase, showing '$TlPb_2I_5$' composition in the two-phase region $TlPbI_3$ + PbI_2. The latter is in agreement with our findings, and we hypothesize that the tetragonal $TlPb_2I_5$ phase is stabilized by replacing a part of I^- ions with smaller Cl^- ions, which is supported by the existence of isostructural $TlPb_2Cl_5$ compound[30,31] and by the ratio of ionic radii A/X to B/X criterion in AB_2X_5 compounds.[24]

The liquidus of the section (Fig. 1A) consists mainly of primary crystallization lines of α-solid solution range (HT-$TlPb_2Br_5$) and a wide extent of γ-solid solution. Further increase of iodine content leads to the formation of a maximum on the peak of primary crystallization at 80 mol% '$TlPb_2I_5$'. The mechanism of the γ-solid solution formation (described in the next section) indicates that the separation of the crystallographic sites of halogens occurs at this composition. Therefore, from crystallographic viewpoint, we can assume a formation of the quaternary compound in this case. Its composition fits the formula $TlPb_2BrI_4$ and melts congruently at 626 K. The section is non-quasi-binary near '$TlPb_2I_5$', due to the absence of the ternary iodide at the stable phase diagram. Since the '$TlPb_2I_5$' composition lies in the field of the primary crystallization of $TlPbI_3$,[32] the liquidus in this vicinity also contains this field. The secondary crystallization is represented by three-phase regions 8 and 9 (Fig. 1A), and the completion of the crystallization in this section takes place on the horizontal line at 600 K, which is a part of the four-phase non-variant process in the system $2TlI + PbBr_2 \leftrightarrow 2TlBr + PbI_2$.

Fig. 1D summarizes the temperature-dependent powder XRD analysis. Thermal expansion of the $TlPb_2Br_5$ lattice leads to a gradual shift of all Bragg reflections to shorter angles at higher temperatures. Furthermore, a phase change of the $TlPb_2Br_5$ structure appears in the temperature vicinity of 290–300 °C, which agrees well with the previously reported data.[26] This phase transition is indicated by many new XRD reflections, *e.g.* at 22.1°, 22.3°, 28.5°, 33.6°, 33.8°, *etc.*

Crystal structure of the $TlPb_2Br_{5-x}I_x$ solid solution

The crystal structure of $TlPb_2Br_{5-x}I_x$ and the mechanism of solid solution formation were determined by X-ray structure analysis. The isostructural $RbPb_2Br_5$ compound was chosen as a starting model for the computations (structure type $NH_4Pb_2Br_5$, space group $I4/mcm$, a = 8.4455 Å, c = 14.591 Å),[19] replacing Rb atoms with Tl. Experimental and calculated diffraction patterns of $TlPb_2Br_{2.5}I_{2.5}$ as well as the residual line are shown in Fig. S3 (ESI†) as an example. Table S3 (ESI†)

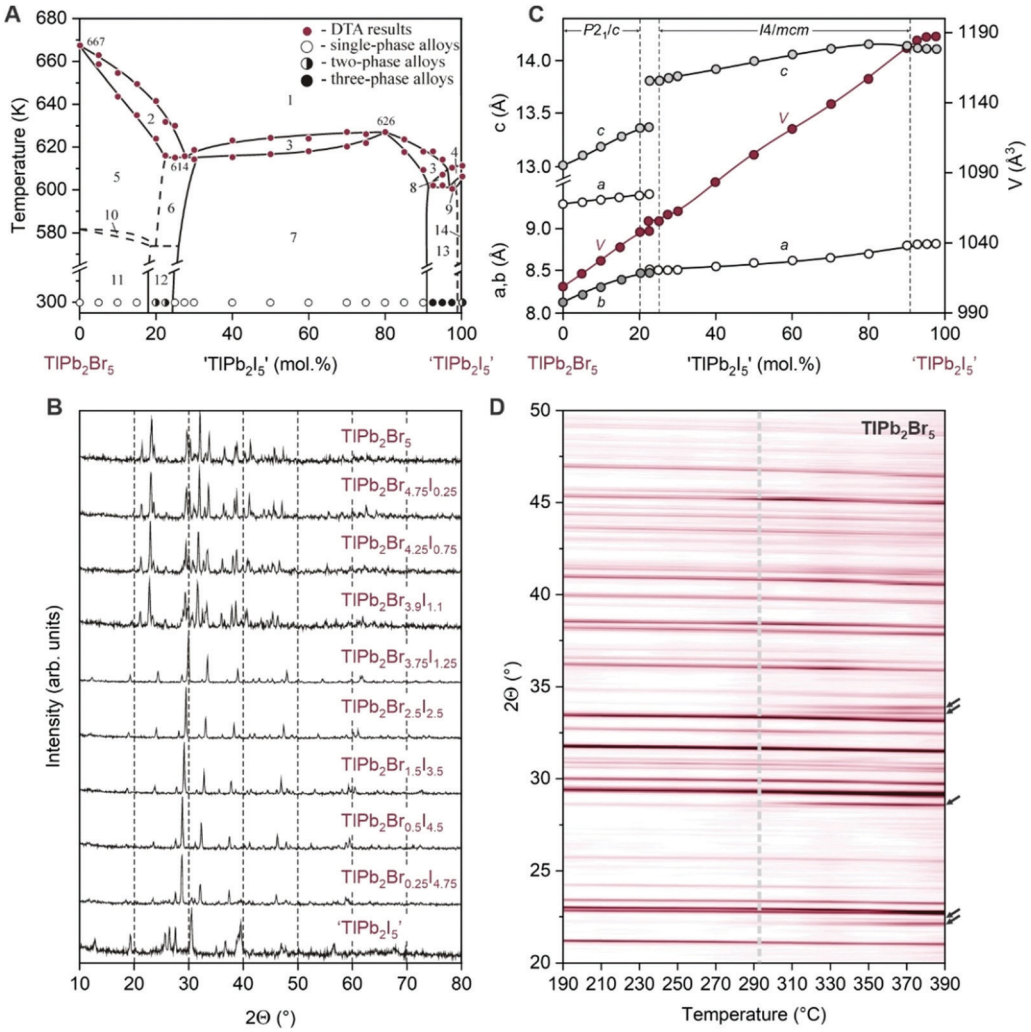

Fig. 1 (A) Phase diagram of the $TlPb_2Br_5$–'$TlPb_2I_5$' section. Numbers indicate the following phase regions: (1) Liquidus (L), (2) L + α, (3) L + γ, (4) L + $TlPbI_3$, (5) α, (6) α + γ, (7) γ, (8) L + γ + $TlPbI_3$, (9) L + $TlPbI_3$ + PbI_2, (10) α′, (11) α + α′, (12) α′ + γ, (13) γ + $TlPbI_3$ + PbI_2, and (14) $TlPbI_3$ + PbI_2. (B) Diffraction patterns of the alloys in the $TlPb_2Br_5$–'$TlPb_2I_5$' section, containing various concentrations of Br and I. (C) Composition-dependent lattice constants for the $TlPb_2Br_5$–'$TlPb_2I_5$' alloys. Solid solution regions within the $TlPb_2Br_5$–'$TlPb_2I_5$' section are marked with vertical dashed lines. (D) High-temperature XRD measurements for the $TlPb_2Br_5$ powder with a temperature increment of 20 °C, presented as a contour plot. Dashed line indicates the temperature of phase transition and arrows point to new reflections for HT-$TlPb_2Br_5$.

summarizes the refinement results of the structure parameters for all 7 alloys, which belong to the $TlPb_2Br_{5-x}I_x$ solid solution with a tetragonal symmetry.

The unit cell and coordination polyhedra of atoms in the $TlPb_2Br_{5-x}I_x$ solid solution are shown for the $TlPb_2BrI_4$ structure in Fig. 2A. The coordination polyhedra for thallium atoms are bi-capped square antiprism [TlI_8Br_2] with a coordination number (CN) of 10. The coordination polyhedra of Pb atoms are trigonal prisms with two additional atoms across the lateral faces [PbI_6Br_2], CN = 8. For halogen atoms, octahedra are typical coordination environments (CN = 6), nearly symmetrical for Br atoms [$BrPb_4Tl_2$], and strongly deformed for I atoms [IPb_3Tl_2I].

Halogen atoms occupy two crystallographic sites: 4c and 16l (Table S3, ESI†). When the iodine content is low, Br atoms occupy the 4c site and statistically share the 16l site with I atoms. As the iodine content increases, the 16l site is first fully replaced, while the 4c site remains filled with Br atoms. In the $TlPb_2BrI_4$ alloy (*i.e.*, $TlPb_2Br_{5-x}I_x$ with $x = 4$), this substitution mechanism results in the separation of the crystallographic sites between the halogen atoms (Table S4 and Fig. S4, ESI†). Further increase of the iodine content leads to the substitution of Br in the 4c site, but the structure becomes unstable after the displacement of half of the Br atoms (*i.e.*, $x > 4.5$ in $TlPb_2Br_{5-x}I_x$).

The crystal structure of the $TlPb_2Br_{5-x}I_x$ solid solution can be presented as the arrangement of halogen atom polyhedra, alternating with the polyhedra of metallic components. The peculiarity of an ordered quaternary structure, $TlPb_2BrI_4$, is that the polyhedra of Tl atoms are surrounded by the polyhedra of Br atoms (Fig. 2B), while the polyhedra of Pb atoms are surrounded by the polyhedra of I atoms (Fig. 2C). The Tl

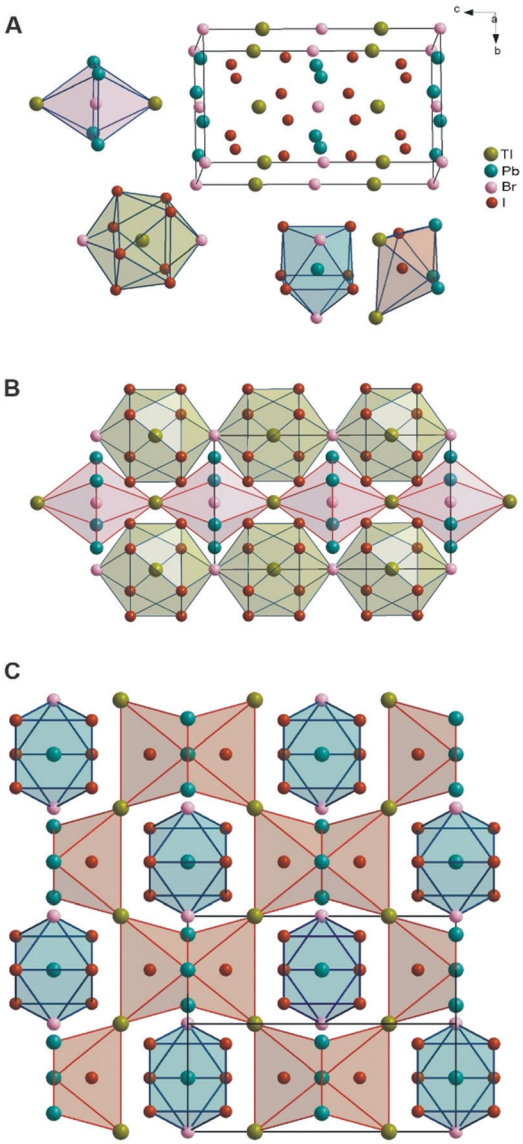

Fig. 2 (A) Unit cell and coordination polyhedra of atoms in the $TlPb_2Br_{5-x}I_x$ solid solution, shown for the case of $TlPb_2BrI_4$. (B) Mutual packing of the polyhedra of Tl and Br atoms in the $TlPb_2BrI_4$ structure. (C) Mutual packing of the polyhedra of Pb and I atoms in the $TlPb_2BrI_4$ structure.

polyhedra are connected by the vertices, forming continuous layers. A layer of Br-centered octahedra forms in the same way and the two layers alternate along the *b*-axis of the unit cell (Fig. 2B). In contrast, polyhedra of Pb atoms are space-isolated and each of them is surrounded by deformed octahedra of I atoms (Fig. 2C).

The substitution of I atoms by Br in the $TlPb_2I_{5-x}Br_x$ phase involves a small shift of atoms within the unit cell and this leads to a decrease of the symmetry from tetragonal to monoclinic in the concentration range between 78 and 82 mol% '$TlPb_2I_5$'. Fig. 3 illustrates a representative understanding of the phase transition mechanism through local distortions, resulting in pronounced octahedral tilting.

X-Ray photoelectron spectroscopy studies

Survey XPS spectra of the $TlPb_2Br_{5-x}I_x$ solid solution were fully indexed to constituent element core-levels or Auger lines (Fig. S5, ESI†). We also observed the C 1s and O 1s levels, due to adsorption of hydrocarbons and oxygen-containing species from prolonged storage in air. However, the intensities of the O 1s line are relatively low (Fig. S5, ESI†), which indicates that quaternary $TlPb_2Br_{5-x}I_x$ single crystals are little hydroscopic. This property is highly demanded for stable operation of $TlPb_2Br_{5-x}I_x$-based devices under ambient conditions.

Typical core-level XPS spectra for the surfaces of $TlPb_2Br_{5-x}I_x$ single crystals are shown in Fig. 4A–C. In agreement with composition, the relative intensities of the Tl 4f and Pb 4f spin–orbit doublets remain constant throughout the $TlPb_2Br_{5-x}I_x$ solid solution, whereas the intensities of Br 3p and I 3d core-levels monotonously change, in accordance. We also report no change of the spin–orbit splitting for I 3d, Tl 4f, Pb 4f and Br 3p core-level spectra in the $TlPb_2Br_{5-x}I_x$ solid solution.

Fig. 4D shows binding energies for I $3d_{5/2}$, Br $3p_{3/2}$, Pb $4f_{7/2}$ and Tl $4f_{7/2}$ core-level spectra as a function of bromine content in the $TlPb_2Br_{5-x}I_x$ solid solution, including the $TlPb_2Br_5$ compound reported by us previously.[16] While binding energies of Pb $4f_{7/2}$ core-level electrons remain constant, binding energies of Tl $4f_{7/2}$ core-level electrons increase towards high Br content $TlPb_2Br_{5-x}I_x$ compounds. This observation is associated with the increase of positive effective charge of Tl atoms, changing from $TlPb_2Br_{0.5}I_{4.5}$ to $TlPb_2Br_5$. Similarly, binding energies of I $3d_{5/2}$ core-level electrons are composition-invariant, while binding energies of Br $3p_{3/2}$ core-level electrons decrease from $TlPb_2Br_{0.5}I_{4.5}$ to $TlPb_2Br_5$, which indicates a more negative charge state of Br atoms in $TlPb_2Br_{5-x}I_x$ compounds with high Br content. Taken together, observed composition dependences of atomic binding energies suggest more ionic nature of $TlPb_2Br_{5-x}I_x$ compounds with high Br content and consequently, their wider band gaps.

Fig. 5A shows XPS valence-band spectra of $TlPb_2Br_{5-x}I_x$ compounds. It is possible to distinguish three fine structures of the valence band (denoted as A, B, and C) for all $TlPb_2Br_{5-x}I_x$ compositions (Fig. 5A). Our previous first-principles calculations of $TlPb_2Br_5$ indicate that the Br 4p states are main contributors to band A of the valence band, while Pb 6s and Tl 6s states build bands B and C.[16] We conclude that the valence bands of $TlPb_2Br_{5-x}I_x$ compounds are built analogously, such that band A consists of the Br 4p and I 5p states. In agreement, we observe a decrease of the relative intensities of band A from $TlPb_2Br_3I_2$ to $TlPb_2Br_{0.5}I_{4.5}$ (Fig. 5A), due to smaller photoionization cross-sections for the I 5p states compared to the Br 4p states.[33]

Electronic structure calculations

We calculate the electronic structure of the quaternary $TlPb_2BrI_4$ compound, using the tight-binding linear muffin-tin orbital (TB–LMTO) method in the atomic spheres approximation.[18] For calculations, we use the experimental crystallographic data (Table S4, ESI†). The total and partial densities of states (DOSs) for $TlPb_2BrI_4$ are

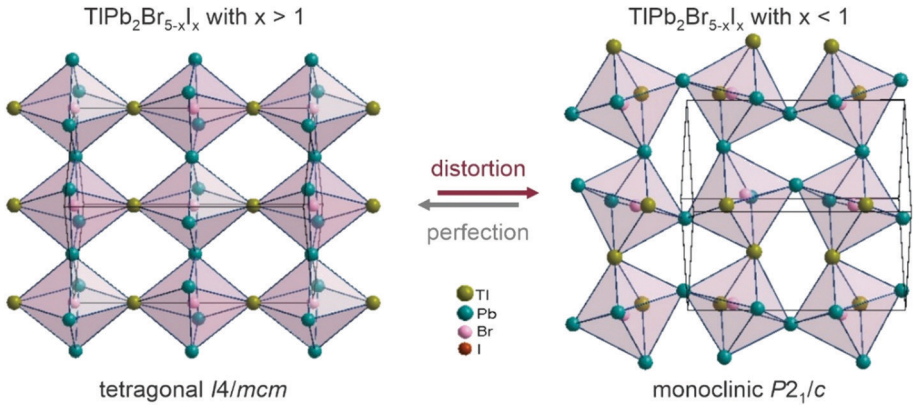

Fig. 3 Changes in the arrangement of the bromine-centred octahedra during structure transformation from tetragonal to monoclinic.

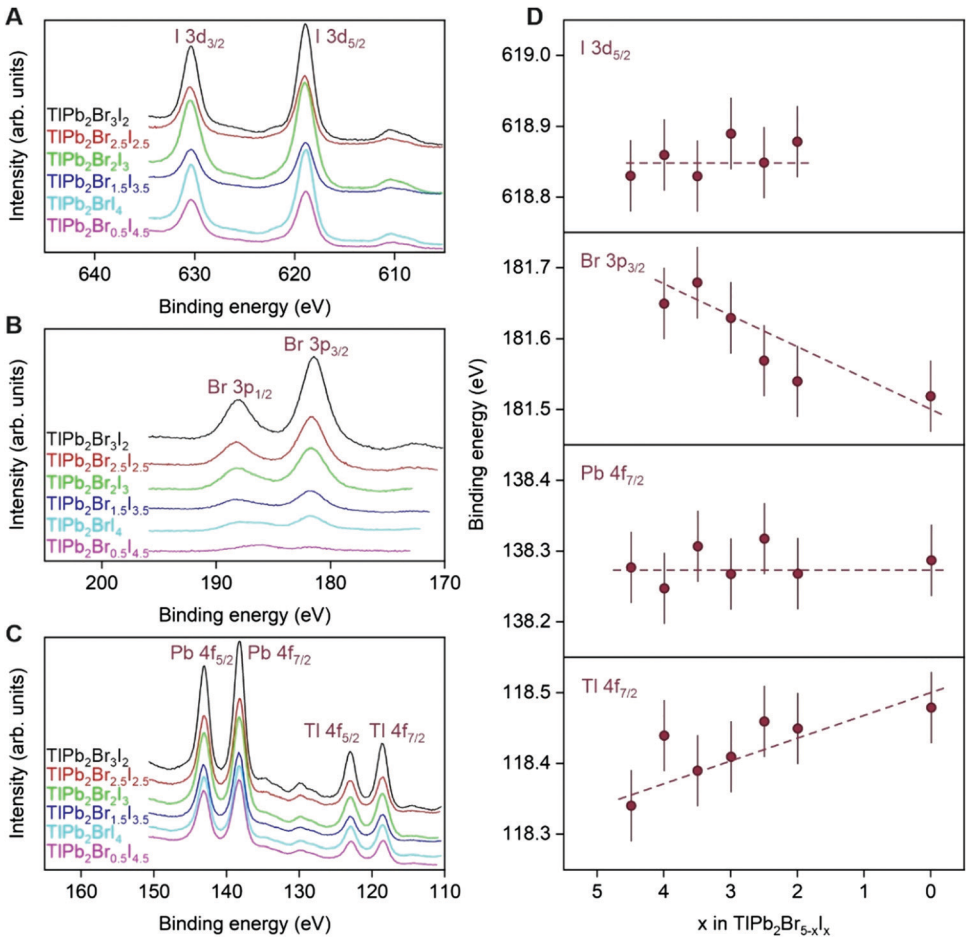

Fig. 4 (A–C) XPS spectra of I 3d, Br 3p, Pb 4f, and Tl 4f core-levels, measured for the $TlPb_2Br_{5-x}I_x$ solid solution. (D) Composition dependences of Tl $4f_{7/2}$, Pb $4f_{7/2}$, Br $3p_{3/2}$, and I $3d_{5/2}$ binding energies in $TlPb_2Br_{5-x}I_x$ compounds.

shown in Fig. 5B. The DOS band gap in the proximity of Fermi energy, E_F, suggests that the quaternary $TlPb_2BrI_4$ compound belongs to wide band gap semiconductors with a band gap energy $E_g > 2$ eV. Comparing calculated DOS with experimental XPS valence-band spectrum (Fig. 5B) reveals a good agreement between the two methods. In particular, the overall shape and energy positions of XPS fine structures can be clearly attributed to the DOS regions within the valence band of the $TlPb_2BrI_4$ semiconductor.

The maximum electron localization function (ELF) for the $TlPb_2BrI_4$ compound appears around halogen atoms (Fig. 5B, inset), while calculated electron localizations around Tl and Pb

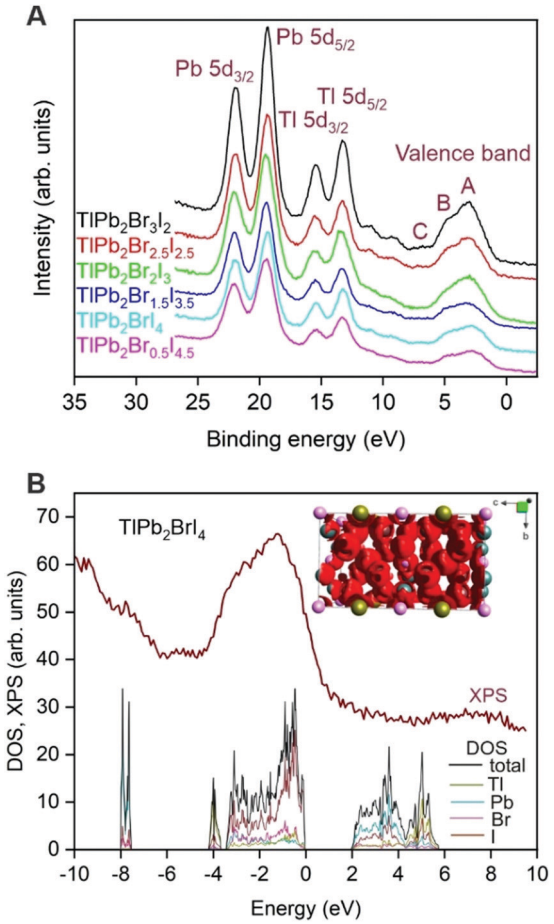

Fig. 5 (A) XPS valence-band spectra measured for the $TlPb_2Br_{5-x}I_x$ solid solution. (B) Total and partial densities of states for the $TlPb_2BrI_4$ crystal, showing in comparison with the XPS valence-band spectrum. Inset B: The iso-surfaces of the electron localization function around atoms in the $TlPb_2BrI_4$ structure.

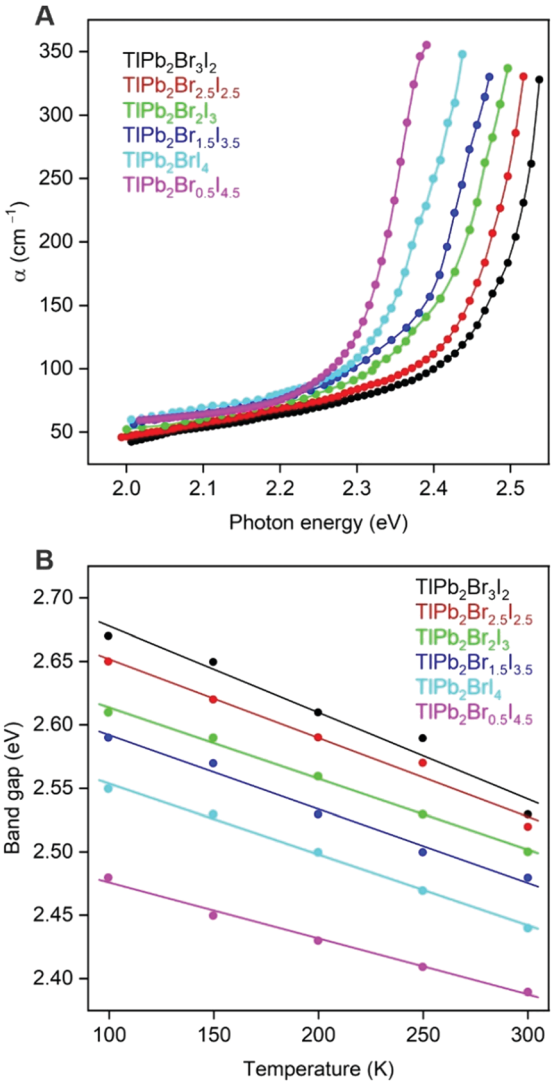

Fig. 6 (A) Absorption spectra for the $TlPb_2Br_{5-x}I_x$ crystals at 300 K and (B) temperature dependence of optical band gap energies for the $TlPb_2Br_{5-x}I_x$ crystals.

atoms are smaller. Apparent shift of the ELF from metals to halogens can be associated with the ionic nature of bonding in the $TlPb_2BrI_4$ compound (*e.g.*, complex $[BrI_4]^{5-}$ anions are compensated by two Pb^{2+} and one Tl^+ cations).

The crystal orbital Hamilton population (COHP) indicates that the strongest interactions exist between I and Pb atoms. For the Pb–I interactions (δ_{Pb-I} =3.076 Å) the integrated COHP ($-iCOHP_{Pb-I}$) is 1.328 eV. The Pb–Br interaction is relatively weaker ($-iCOHP_{Pb-Br}$ = 0.443 eV), while the Pb–Br distance is larger (δ_{Pb-Br} = 3.230 Å). The distances between Tl and halogens are notably larger than that for Pb and halogens (δ_{Tl-I} = 3.690 Å and δ_{Tl-Br} = 3.813 Å), which cause relatively weaker interactions of Tl with halides ($-iCOHP_{Tl-I}$ = 0.251 eV and $-iCOHP_{Tl-Br}$ = 0.071 eV).

Optical properties

Absorption spectra of the $TlPb_2Br_{5-x}I_x$ compounds were collected in the temperature range of 100–300 K (Fig. 6). All investigated $TlPb_2Br_{5-x}I_x$ compounds are typical wide-gap semiconductors, whose band gap energy (E_g) varies with composition, narrowing with an increase of the I content in the $TlPb_2Br_{5-x}I_x$ solid solution. For example, at room temperature, E_g of $TlPb_2Br_3I_2$ is 2.53 eV, while E_g of $TlPb_2Br_{0.5}I_{4.5}$ is 2.39 eV (Fig. 6B). Such composition dependence of E_g agrees well with our electronic structure calculations and the color of the synthesized $TlPb_2Br_{5-x}I_x$ single crystals (Fig. S1, ESI†). Decreasing temperature widens the energy band gaps of $TlPb_2Br_{5-x}I_x$ monotonously and E_g of $TlPb_2Br_3I_2$ becomes 2.67 eV, while E_g of $TlPb_2Br_{0.5}I_{4.5}$ becomes 2.48 eV (Fig. 6B).

The $TlPb_2Br_{5-x}I_x$ semiconductors have a large concentration of defects, which is indicated by low-energy tails of the fundamental absorption edges (Fig. 6A). The tails exhibit a similar slope for all $TlPb_2Br_{5-x}I_x$ compositions, which can be fit with the Urbach rule for the disordered systems.[34] Characteristic energy Δ (*i.e.*, a degree of crystal lattice disorder)[35] attains large values of 0.08–0.10 eV for the $TlPb_2Br_{5-x}I_x$ compound, approaching the Δ values of amorphous systems. This indicates

the prevailing role of the static disorder in the $TlPb_2Br_{5-x}I_x$ compounds, *e.g.* by the fluctuation of charged defect concentration to modulate the electric field randomly and thus distort the periodicity of the electron potential.

Conclusions

In this paper, we have investigated the phase diagram of the $TlPb_2Br_5$–'$TlPb_2I_5$' section, based on 21 alloys. We have discovered a new quaternary compound with a composition of $TlPb_2BrI_4$. This mixed halogenide is indexed in the tetragonal structure (space group *I4/mcm*, structure type $NH_4Pb_2Br_5$). $TlPb_2BrI_4$ melts congruently at 626 K, and has a wide homogeneity region in the range of 24–91 mol% '$TlPb_2I_5$'. The $TlPb_2BrI_4$ solid solution forms *via* gradual substitution of Br by I on the 16l site, while the 4c Br site can be substituted only partially and only after complete substitution of Br by I on the 16l site. We have also revealed the existence of high-temperature $TlPb_2Br_5$ modification, stable above a phase change temperature of 290–300 °C.

We have grown six $TlPb_2Br_{5-x}I_x$ single crystals by the Bridgman-Stockbarger method with composition varying from $TlPb_2Br_2I_3$ to $TlPb_2Br_{0.5}I_{4.5}$. The structure and properties of these single crystals are studied by X-ray photoelectron spectroscopy, X-ray diffraction, and absorption spectroscopy. We have also performed the electronic structure calculations for the $TlPb_2BrI_4$ compound, using the tight-binding linear muffin-tin orbital method.

Our results offer new compositions, showing potential for room-temperature X-ray and γ-ray photodetectors. Our approach involves the development of new materials *via* continuous substitution of simple compositions. This strategy can be successfully applied *e.g.* for a series of quinary $Cu_2BaGe_{1-x}Sn_xSe_4$ alloys ($0 \leq x \leq 1$) to fine-tune the structural, optical, and electronic properties for photovoltaic applications.[36]

Author contributions

O. V. P. conceived the study. All authors contributed to data curation, analysis, or investigation. O. V. P., M. P., and M. Y. wrote the original manuscript with input from all authors. M. Y. reviewed and edited the manuscript with input from M. P., O. Y. K., V. P., and A. O. F.

Conflicts of interest

There are no conflicts to declare.

Acknowledgements

This work was partially supported by the Ministry of Science and Higher Education of Poland (project No 16.16.160.557). M.Y. acknowledges financial support from the Swiss National Science foundation *via* an Ambizione Fellowship (No. 161249). This article is dedicated to the memory of Professor Oleg Parasyuk, Dean of Department of Inorganic and Physical Chemistry, Eastern European National University (Lutsk, Ukraine), who passed away suddenly in December 2018.

References

1 S. Wang, Z. Liu, J. A. Peters, M. Sebastian, S. L. Nguyen, C. D. Malliakas, C. C. Stoumpos, J. Im, A. J. Freeman, B. W. Wessels and M. G. Kanatzidis, *Cryst. Growth Des.*, 2014, **14**, 2401–2410.
2 F. Zhang, Z. He and C. Seifert, *IEEE Trans. Nuclear Sci.*, 2007, **54**, 843–848.
3 T. E. Schlesinger and R. B. James, *Semiconductors for Room Temperature Nuclear Detector Applications*, Academic Press, New York, 1995.
4 B. Donmez, C. L. Thrall, H. Zhong, L. J. Cirignano, K. Hadong and K. S. Shah, *IEEE Nuclear Sci. Symposium*, 2010, **1**, 3773.
5 D. Nason and L. J. Keller, *J. Cryst. Growth*, 1995, **156**, 221–226.
6 W. Li, Z. Li, S. Zhu, S. Yin, B. Zhao and G. Chen, *Nucl. Instrum. Methods Phys. Res., Sect. A*, 1996, **370**, 435–437.
7 Y. He, S. Zhu, B. Zhao, Y. Jin, Z. He and B. Chen, *J. Cryst. Growth*, 2007, **300**, 448–451.
8 T. Hayashi, M. Kinpara, J. F. Wang, K. Mimura and M. Isshiki, *J. Cryst. Growth*, 2008, **310**, 47–50.
9 C. C. Stoumpos, C. D. Malliakas, J. A. Peters, Z. Liu, M. Sebastian, J. Im, T. C. Chasapis, A. C. Wibowo, D. Y. Chung, A. J. Freeman, B. W. Wessels and M. G. Kanatzidis, *Cryst. Growth Des.*, 2013, **13**, 2722–2727.
10 Z. Liu, J. A. Peters, C. C. Stoumpos, M. Sebastian, B. W. Wessels, J. Im, A. J. Freeman and M. G. Kanatzidis, *Proc. SPIE*, 2013, **8852**, A-1–A-7.
11 S. Johnsen, Z. Liu, J. A. Peters, J.-H. Song, S. Nguyen, C. D. Malliakas, H. Jin, A. J. Freeman, B. W. Wessels and M. G. Kanatzidis, *J. Am. Chem. Soc.*, 2011, **133**, 10030–10033.
12 Z. Liu, J. A. Peters, S. Nguyen, M. Sebastian, B. W. Wessels, S. Wang, H. Jin, J. Im, A. J. Freeman and M. G. Kanatzidis, *Proc. SPIE*, 2012, **8507**, O-1–O-9.
13 A. V. Churilov, G. Ciampi, H. Kima, W. M. Higgins, L. J. Cirignano, F. Olschner, V. Biteman, M. Minchello and K. S. Shah, *J. Cryst. Growth*, 2010, **312**, 1221–1227.
14 K. S. Shah, J. C. Lund, F. Olschner, J. Zhang, L. P. Moy, M. R. Squillante, W. W. Moses and S. E. Derenzo, *IEEE Trans. Nuclear Sci.*, 1994, **41**, 2715–2718.
15 U. Hömmerich, E. Brown, A. Kabir, D. Hart, S. B. Trivedi, F. Jin and H. Chen, *J. Cryst. Growth*, 2017, **479**, 89–92.
16 O. Y. Khyzhun, V. L. Bekenev, N. M. Denysyuk, I. V. Kityk, P. Rakus, A. O. Fedorchuk, S. P. Danylchuk and O. V. Parasyuk, *Opt. Mater.*, 2013, **36**, 251–258.
17 J. Rodriguez-Carvajal, *Physica B*, 1993, **192**, 55–69.
18 O. Jepsen, A. Burkhardt and O. K. Andersen, *The TB-LMTO-ASA Program, version 4.7; Max-Planck Institut für Festkörperforschung: Stuttgart*, Germany, 1999.
19 S. Rajagopal, D. Nataraj, O. Y. Khyzhun, Y. Djaoued, J. Robichaud and C.-K. Kim, *Mater. Chem. Phys.*, 2013, **141**, 383–392.

20 O. Y. Khyzhun, V. L. Bekenev, O. V. Parasyuk, S. P. Danylchuk, N. M. Denysyuk, A. O. Fedorchuk, N. Al-Zayed and I. V. Kityk, *Opt. Mater.*, 2013, **35**, 1081–1089.
21 N. M. Denysyuk, V. L. Bekenev, M. V. Karpets, O. V. Parasyuk, S. P. Danylchuk and O. Y. Khyzhun, *J. Alloys Compd.*, 2013, **576**, 271–278.
22 O. Y. Khyzhun, P. M. Fochuk, I. V. Kityk, M. Piasecki, S. I. Levkovets, A. O. Fedorchuk and O. V. Parasyuk, *Mater. Chem. Phys.*, 2016, **172**, 165–172.
23 D. Briggs and P. M. Seach, *Practical Surface Analysis: Auger and X-Ray Photoelectron Spectroscopy*, John Willey & Sons Ltd, Chichester, 2nd edn, 1990, vol. 1.
24 H. I. Beck, G. Clique and H. Nau, *Z. Anorg. Allg. Chem.*, 1986, **536**, 36–44.
25 M. Cola, V. Masarotti, R. Riccardi and C. Sinistri, *Z. Naturforsch., A: Astrophys., Phys. Phys. Chem.*, 1971, **26**, 1328–1332.
26 V. B. Lazarev, E. Y. Peresh, V. V. Tsigika, V. M. Chereshnya, V. S. Diordyai and N. P. Stasyuk, *Zh. Neorg. Khim.*, 1982, **27**, 2943–2947.
27 M. Shklovskaya, S. M. Arkhipov, V. A. Kuzina and T. E. Vdorkina, *Russ. J. Inorg. Chem.*, 1983, **28**, 1058.
28 E. Y. Peresh, V. B. Lazarev, V. V. Tsigika, Y. V. Voroshilov and V. S. Diordyai, *Zh. Neorg. Khim.*, 1980, **25**, 1368–1371.
29 S. I. Levkovets, P. M. Fochuk, A. O. Fedorchuk, L. V. Piskach and O. V. Parasyuk, *Nauk. Visnyk Chernivtsi Univ.*, 2015, **753**, 108–112.
30 H.-L. Keller, *J. Solid State Chem.*, 1983, **48**, 346–350.
31 O. Y. Khyzhun, V. L. Bekenev, N. M. Denysyuk, O. V. Parasyuk and A. O. Fedorchuk, *J. Alloys Compd.*, 2014, **582**, 802–809.
32 S. I. Levkovets, P. M. Fochuk, A. O. Fedorchuk, L. V. Piskach, I. D. Olekseyuk and O. V. Parasyuk, *Nauk. Visnyk Chernivtsi Univ.*, 2016, **781**, 54–59.
33 M. Ikedo, M. Watari, F. Tateishi and H. Ishiwatari, *J. Appl. Phys.*, 1986, **60**, 3035.
34 O. Y. Khyzhun, I. V. Kityk, M. Piasecki, A. O. Fedorchuk, S. I. Levkovets, P. M. Fochuk, G. L. Myronchuk and O. V. Parasyuk, *Phys. B*, 2015, **479**, 134–142.
35 M. G. Brik, I. V. Kityk, N. M. Denysyuk, O. Y. Khyzhun, S. I. Levkovets, O. V. Parasyuk, A. O. Fedorchuk and G. L. Myronchuk, *Phys. Chem. Chem. Phys.*, 2014, **16**, 12838–12847.
36 G. C. Wessler, T. Zhu, J.-P. Sun, A. Harrell, W. P. Huhn, V. Blum and D. B. Mitzi, *Chem. Mater.*, 2018, **30**, 6566–6574.